

PAPER

Understanding the chemical reactions in cathodic plasma electrolysis

To cite this article: Bocong Zheng *et al* 2019 *Plasma Sources Sci. Technol.* **28** 085016

View the [article online](#) for updates and enhancements.



IOP | ebooksTM

Bringing you innovative digital publishing with leading voices to create your essential collection of books in STEM research.

Start exploring the **collection** - download the first chapter of every title for free.

Understanding the chemical reactions in cathodic plasma electrolysis

Bocong Zheng¹ , Keliang Wang¹, Maheshwar Shrestha¹, Thomas Schuelke^{1,2} and Qi Hua Fan^{1,2,3}

¹Fraunhofer Center for Coatings and Diamond Technologies, Michigan State University, East Lansing, MI 48824, United States of America

²Department of Electrical and Computer Engineering, Michigan State University, East Lansing, MI 48824, United States of America

³Department of Chemical Engineering and Materials Science, Michigan State University, East Lansing, MI 48824, United States of America

E-mail: qfan@egr.msu.edu

Received 7 May 2019, revised 9 July 2019

Accepted for publication 29 July 2019

Published 20 August 2019



Abstract

Plasma electrolysis (PE) combines the characteristics of electrolysis and plasma discharges, creating high-energy-density plasmas that lead to intensive physical processes and chemical reactions on the working electrode. The authors have found that the physical processes and the chemical reactions could be decoupled under certain conditions, and a textured electrode surface could be created through a chemical-reaction-dominated process instead of an irregular porous surface produced by the physical-dominated interactions. A plasma fluid model for the chemical-reaction-dominated discharge is established with constraint conditions obtained from the experiments. This study aims to elucidate the plasma characteristics and the chemical reactions in cathodic PE. The modeling reveals that the plasma is highly electronegative, and the dominant neutral species are H₂ and O₂ dissociated from water vapor. The decoupling mechanism is attributed to the low surface tension, high viscosity and high boiling point of glycerol in the electrolyte, which suppress the localized intensive physical interactions and promote the formation of a stable vapor layer. The formation of textured surface is attributed to the anisotropic chemical etching by the reactive species generated in the plasmas.

Keywords: plasma model, plasma electrolysis, contact glow discharge electrolysis

1. Introduction

Plasma electrolysis (PE), also termed contact glow discharge electrolysis [1–3], is a novel electrolysis in which an electrode is submerged in a liquid electrolyte and a plasma is formed in a vapor layer around the electrode. PE discharges can be obtained by applying a sufficiently high voltage between the electrode (either cathode or anode) and the liquid electrolyte, so that a normal electrolysis breaks down and a plasma is formed and sustained by dc glow discharges. The solvent vaporization near an electrode by Joule heating and the onset of Taylor–Helmholtz hydrodynamic instability have been suggested as the primary reasons for the breakdown of normal electrolysis [1, 3, 4]. PE combines the characteristics of electrolysis and plasma discharge. The high energy density in PE discharge leads to intensive physical processes and

chemical reactions on the working electrode, which makes it an efficient way for nanomaterial synthesis [5–7], surface modification [8] and surface cleaning [9].

Kellogg [10] performed the first significant research on PE phenomenon, followed by the study of Hickling and Ingram [11] on glow discharge in PE. These pioneering works led to subsequent studies of both basic research and practical applications of PE. A large amount of these studies have focused on physical interactions between the plasma and the working electrode, which are caused by the implosion of plasma bubbles [9, 12]. For example, in a typical cathodic PE, the high electric potential drop between the cathode and the electrolyte results in a high concentration of positive ions in the electrolyte in close proximity to the cathode, establishing a strong localized electric field up to $\sim 10^5$ V m⁻¹ and causing intensive gas ionization [8, 13]. The plasma temperature can

locally reach as high as several thousands Kelvin [12], resulting in a rapid expansion of the plasma bubble. Once the plasma bubble collapsed due to electrolyte quench, the stored energy is released, the kinetic energy is transferred to the working surface as microscale impact, creating relatively large and non-uniform particles with sizes ranging from 100 nm to 2 μ m [5], and altering the working surface to an irregular porous morphology [12, 14].

Besides the broad research on the physical processes in PE, the plasma chemistry has been investigated as well [15–17]. The chemical reactions induced by the high-energy-density plasma exist in and between multiple phases (plasma-electrode, plasma-electrolyte, plasma-gas). Compared to conventional gas-phase discharge, the chemical reactions in PE are more complicated and create rich sources of radicals, such as OH, O and H₂O₂, as well as electromagnetic radiation [18]. A strong deviation of the chemical yield from the estimation based on Faraday law has also been observed in PE [19, 20]. These non-faradaic yields originate in two separate reaction zones, the plasma phase reaction zone and the liquid phase reaction zone, and in each of the reaction zones the non-faradaic products dissociated from the water vapor and liquid water molecules satisfy the mass balance [3]. The excess gas evolution can be detected at either the cathode or the anode, although in cathodic PE the non-faradaic effect is significantly reduced [1, 19], about 75% of the yield originates from the plasma phase and 25% from the liquid phase, contrary to the anodic PE [3].

The previous studies indicate that complex physical interactions and chemical reactions between the electrode and the electrolyte occur simultaneously and in concert, and PE appears to be dominated by physical processes, as evidenced by the irregular porous morphology created on the surface of anisotropic crystals [12]. Plasma-liquid interactions in PE discharges have been investigated using imaging [21] and optical emission spectroscopy [14, 22, 23], and some basic plasma parameters including plasma chemical species, electron density and temperature are measured. However, further understanding of the plasma-liquid interaction and the underlying mechanism of PE discharges requires modeling. Due to the complicated physical processes and chemical reactions in PE discharges, it is difficult to develop a model that includes all the details. To the best of the authors' knowledge, only the phenomenological model [24] that treats the discharge process as a black box, or the electro-fluid model [21] that describes the vapor layer dynamics have been reported, no models dealing with fundamental plasma discharges and chemical reactions in PE have been developed so far. Fortunately, recent findings suggest that under certain conditions, the physical processes and the chemical reactions can be decoupled in PE discharges [25]. This makes it possible to model only the chemical reactions in PE discharges.

This work aims to elucidate the plasma characteristics and the chemical reactions of cathodic PE discharges from a modeling point of view. This paper is organized as follows. In section 2, the experimental apparatus is illustrated, the discharge voltages and currents are provided as the input parameters of the model. In section 3, a plasma fluid model that

describes the chemical reactions of cathodic PE discharges is developed, the boundary conditions for different kinds of species, the chemical reaction set used in the model, and the numerical procedure of calculation are provided in detail. In section 4, the calculated electron density, electron temperature, electric potential and the number densities of different species are presented as a base case simulation, the influence of the uncertainty of some input parameters on the modeling results is investigated. Furthermore, the decoupling mechanisms of physical processes and chemical reactions in cathodic PE, and the chemical etching mechanisms on the electrode surface are discussed. Finally, the conclusions are given in section 5.

2. Experimental apparatus

The experimental setup of a cathodic PE is illustrated in figure 1. A 250 ml stainless steel beaker was grounded as the anode, the diameter was 65 mm and the height was 80 mm. A tungsten wire of diameter 2 mm and length of 1 cm, or a mirror polished n-type (100) silicon wafer of dimensions 25 mm \times 6 mm \times 0.65 mm were used as working cathodes. The cathodes were positioned at the center of the beaker and connected to a negative DC power. For the tungsten wire and the silicon wafer cathodes, about 5 mm and 13 mm were immersed into the electrolyte solution, respectively. The electrolyte solution was composed of deionized water, glycerol and sodium bicarbonate (NaHCO₃) of 1 wt%. The volume ratio of glycerol to water varied from 0 to 40:1. The electrolyte solution was preheated to 70 °C before the experiment. The glycerol can be used as a practical additive in PE, e.g. to fabricate DLC coatings on carbon steel [26]. However, in this work, the purpose of using high glycerol–water ratio solution is to decouple the physical processes and the chemical reactions in PE. Details can be found in section 4.4.

The discharge current–voltage characteristics of the cathodic PE with a tungsten wire cathode is shown in figure 2. The discharge was excited by a Kikusui PAN 600-2A DC power supply. Under low voltages, up to 75 V, the current increases linearly with the voltage, following the Faraday law. This regime is accompanied by the liberation of small gas bubbles at the tungsten wire and the beaker surface. As increasing the voltage from 75 V to about 170 V, the local vaporization of the electrolyte adjacent to the cathode, induced by Joule heating, leads to the coalescence of fine bubbles at the tungsten cathode. Since the resistance of the vapor layer is much higher than the electrolyte, most of the electric potential drops over the vapor, inducing a strong electric field and resulting in the electric breakdown. The unstable discharge in this regime is evidenced by a significant current oscillation. The fluctuation-averaged current decreases continuously from 2.7 A at 75 V to about 0.3 A at around 170 V. When the voltage reaches 170 V, a continuous vapor layer is formed around the cathode, characterized by the significant drop in current before 170 V. For voltages higher than 170 V, the discharge state becomes stable, the current is

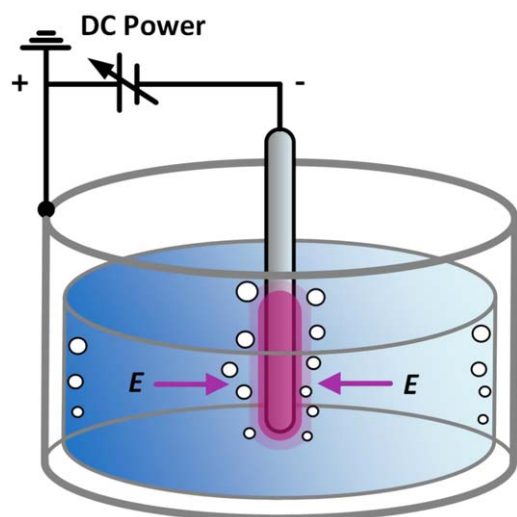


Figure 1. Schematic diagram of the cathodic plasma electrolysis.

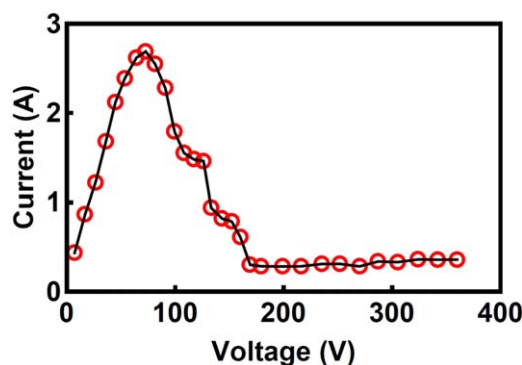


Figure 2. Current–voltage characteristics from normal electrolysis to cathodic PE with a tungsten wire cathode of 2 mm in diameter, of which 5 mm of the wire was immersed in a 1 wt% NaHCO_3 electrolyte with a glycerol to water volume ratio of 10:1, the electrolyte temperature was 70 °C.

independent of the voltage and remains at around 0.3 A. A decoupling of physical processes and chemical reactions has been observed in this regime [25], which will be discussed in section 4.4. With a further increase in voltage to more than 300 V, the discharge reveals intense arcing, meaning that the discharge is dominated by physical processes.

3. Model description

When a liquid is in contact with a surface significantly hotter than the boiling point of the liquid, a thin vapor layer is formed to prevent the liquid from boiling rapidly. This phenomenon is coined as film boiling, and the temperature which indicates the onset of stable film boiling is termed as Leidenfrost temperature. In the stable discharge regime of cathodic PE, due to the strong Joule heating effect, the electrode temperature could be significantly higher than the electrolyte. In that case, the formation of a continuous vapor layer is expected to separate the electrode and the electrolyte.

Table 1. Properties of water and glycerol at 293 K.

| | Surface tension (mN m^{-1}) | Density (g cm^{-3}) | Viscosity (mPa s) |
|----------|-------------------------------------------|-----------------------------------|---------------------------------|
| Water | 72.80 | 0.998 | 1.002 |
| Glycerol | 64.00 | 1.261 | 1412 |

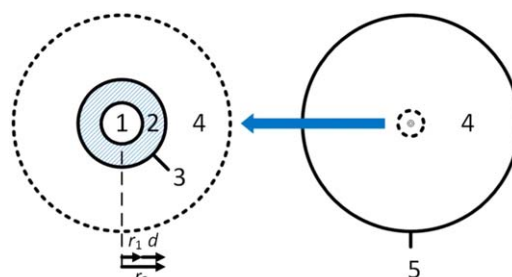


Figure 3. Structure of the 1D plasma fluid model for cathodic PE: 1-the wire cathode, 2-the vapor layer, 3-the plasma-liquid interface, 4-the electrolyte, 5-the beaker anode. r_1 and r_2 are the radius of the wire cathode and the vapor layer, d is the thickness of the vapor layer.

The Leidenfrost temperatures of tungsten and silicon in water are around 543 K [27, 28]. Compared to water, glycerol has lower surface tension and higher density (see table 1). The Leidenfrost temperature of a glycerol/water mixture is therefore expected to be reduced [29], much lower than the boiling point of glycerol 563 K. The Henry's constant of glycerol is not considered. However, from the earlier experimental research [30], for a glycerol–water system with a volume ratio of 10:1, from its isotropic vapor-liquid equilibrium, the vapor fraction of glycerol at the boiling point of the solution is only about 1%. Therefore, it is assumed here that insignificant amounts of glycerol are transported into the vapor phase, and glycerol-related reactions are not considered in the model. The NaHCO_3 has been inferred not to play a major role in chemical reactions of cathodic PE [25], so it is not considered in the model for simplicity. It is assumed that only water vapor exists in the vapor layer. Further discussion about the physical processes and chemical reactions in cathodic PE can be found in section 4.4.

The configuration of the cathodic PE with a tungsten wire cathode is adopted in the model, because the wire cathode is simpler in geometry and can be described in a one-dimensional cylindrical coordinate. The structure of the 1D plasma fluid model for cathodic PE is illustrated in figure 3. A continuous and steady vapor layer is assumed as the simulation region, which is the case for the stable discharge in the voltage range from 170 to about 300 V. The right-hand side is the schematic top-view of the experimental setup, the left-hand side is the magnification of the wire cathode and the vapor layer. Due to the periodical expansion and shrinkage of the vapor layer, the layer thickness is not a constant, in the range of dozens to hundreds of μm [21]. However, the oscillation period of the vapor layer of several ms is sufficient to fully develop the plasma, and the amplitude of the vapor layer of the oscillation is less than 10%. The plasma-liquid

interface is therefore assumed to be fixed during each simulation, although its position can be changed for different simulations to investigate the discharge characteristics and the chemical reactions at different vapor layer thicknesses. The plasma fluid model includes the continuity equations for each species considered in the model, the energy conservation equation for the electrons, and the Poisson's equation. These equations are solved by the commercial software, Comsol Multiphysics [31], and are described in detail as follows.

3.1. Species continuity equation

The continuity equation based on the drift-diffusion approximation for each species except H₂O is

$$\frac{\partial n_j}{\partial t} + \nabla \cdot \Gamma_j = R_j - k_{\text{loss}} n_j, \quad (1)$$

where n_j , Γ_j and R_j are the number density, flux and source term of species j , k_{loss} is the loss rate of neutral species to the ambient air. The drift-diffusion flux of species j is

$$\Gamma_j = z_j \mu_j n_j \mathbf{E} - \nabla (D_j n_j), \quad (2)$$

where z_j , μ_j and D_j are the charge number, mobility and diffusion coefficient of species j , \mathbf{E} is the electric field. The electron mobility μ_e depends on the composition of the neutral gas. In our simulation, only water vapor exists initially, and in addition, there should be H₂, O₂ as well as a small amount of H₂O₂ dissociated from water when the discharge is stable. According to the mass conservation in the plasma reaction zone [3], the concentration of H₂ should be twice of O₂. Since water keeps vaporizing from the electrolyte, the primary neutral species in the vapor layer around the cathode is expected to be H₂ and/or H₂O. Since the electron mobility in water vapor [32] is similar to the electron mobility in H₂ [33], the electron mobility in a mixture of water vapor and H₂ is set as $0.37 \times 10^6 \text{ cm}^2 \text{ Torr V}^{-1} \text{ s}^{-1}$. The diffusion coefficient of electrons is calculated from Einstein's relationship

$$D_e = \mu_e T_e, \quad (3)$$

where T_e is the electron temperature. The source term of species j is

$$R_j = \sum_k \left[(a_{jk}^R - a_{jk}^L) k_k \prod_l n_l^{L_l} \right], \quad (4)$$

where a_{jk}^R and a_{jk}^L are the right-hand side and left-hand side stoichiometric coefficients of species j in reaction k , k_k is the corresponding rate coefficient, and $n_l^{L_l}$ is the number density of the l species in the left-hand side of reaction k . The rate coefficients can be found in table 3. The diffusion coefficients for heavy species is calculated as [34]

$$D = \frac{1 - w_i}{\sum_{j \neq i} \frac{x_j}{D_{ij}}}, \quad (5)$$

where w_i and x_j are the mass fraction of the i species and the mole fraction of the j species, respectively, D_{ij} is the binary diffusion coefficient of i in j , computed from the kinetic gas theory [34]. The corresponding ion mobilities are calculated from Einstein's relation.

A loss term $-k_{\text{loss}} n_j$ is added at the end of equation (1) to take into account the loss of neutral species. Since the discharge system is not closed, the neutral species are losing to the ambient air above the liquid level during the discharge. On the other hand, the electrolyte is vaporized, providing H₂O to the vapor layer and maintaining the pressure at atmospheric pressure. In that case, the number density of water vapor is not calculated from the continuity equation, but obtained from the mass conservation, that the H₂O density equals to the total number density minus the sum density of other species

$$n_{\text{H}_2\text{O}} = n_{\text{tot}} - \sum_{j \neq \text{H}_2\text{O}} n_j, \quad (6)$$

where the total number density depends on the working pressure and gas temperature

$$n_{\text{tot}} = \frac{p}{k_B T_g}, \quad (7)$$

where $p = 1 \text{ atm}$ is the atmospheric pressure, k_B is the Boltzmann constant and T_g is the gas temperature. The loss rate of each neutral species is assumed to be proportional to its density, the corresponding loss rate coefficient is k_{loss} . The determination of k_{loss} requires the knowledge of hydrodynamic behavior and heat transfer during the discharge. However, a more convenient way to determine k_{loss} is to set it as a fitting parameter and obtain it from experimentally measured gas yields. Further details on the influence of k_{loss} can be found in section 4.2.2.

3.2. Electron energy conservation and Poisson's equation

The energy conservation equation for electrons is

$$\frac{\partial n_\epsilon}{\partial t} + \nabla \cdot \Gamma_\epsilon + \mathbf{E} \cdot \Gamma_e = Q, \quad (8)$$

where

$$n_\epsilon = n_e \epsilon \quad (9)$$

and

$$\Gamma_\epsilon = -\mu_\epsilon n_\epsilon \mathbf{E} - \nabla (D_\epsilon n_\epsilon) \quad (10)$$

are the electron energy density and flux, $\epsilon = \frac{3}{2} T_e$ is the electron energy. The electron energy mobility and diffusion coefficient are

$$\mu_\epsilon = \frac{5}{3} \mu_e \quad (11)$$

and

$$D_\epsilon = \frac{5}{3} D_e, \quad (12)$$

respectively. The energy variation due to polarization scattering and inelastic collisions, Q , is

$$Q = \sum_j k_j n_j n_e \Delta \epsilon_j, \quad (13)$$

where k_j and $\Delta \epsilon_j$ are the reaction rate and energy variation of elastic and inelastic collisions between electron and species j . The electric field \mathbf{E} and potential φ can be obtained by

solving the Poisson's equation

$$\mathbf{E} = -\nabla\varphi, \quad (14)$$

and

$$\nabla^2\varphi = \frac{e}{\epsilon_0} \left(\sum_i n_i - n_e \right), \quad (15)$$

where n_i is the number density of ion species i .

Generally, the reaction rate coefficients of electron-impact reactions can be obtained from the cross-sectional data as

$$k_j = \gamma \int_0^\infty \epsilon \sigma_j(\epsilon) f(\epsilon) d\epsilon, \quad (16)$$

where $\gamma = \sqrt{2e/m_e}$ is a constant, m_e is the electron mass, $\sigma_j(\epsilon)$ is the electron-impact cross section with species j , and $f(\epsilon)$ is the electron energy distribution function (EEDF). Zero-dimensional Boltzmann solvers (such as BOLSIG+ [35]) are widely used in determining the EEDF as well as the transport and rate coefficients for electrons [36–41]. Verma *et al* [42] has demonstrated that for the microdischarges operated at 100 s Torr to atmospheric pressure with gap sizes of 100 s μm , which have a similar pressure and gap size to the cathodic PE discharge but driven by a microwave source, fluid simulations using the rate constants from BOLSIG+ showed excellent agreement with kinetic simulations [42]. However, a significant under-prediction of plasma density was observed from a comparison of fluid model and kinetic simulations [42, 43] when the microdischarge is operated under DC regime, due to the high-energy tail of EEDF caused by the secondary electrons accelerated in the DC sheath could not be accounted for in the fluid simulations. In that case, one can use Maxwellian electrons for the DC plasma simulation [44], which agreed well with kinetic simulations under high pressures [42], or use Boltzmann's equation to obtain the EEDF and Monte Carlo simulation to track the secondary electron beam emitted from the cathode [45, 46]. Due to the relatively large chemical reaction set adopted in the model, Monte Carlo simulation will be very time-consuming, therefore the electrons are assumed to be Maxwellian in this model.

3.3. Boundary conditions

The secondary electron emission due to positive ions striking the cathode is considered by an empirical formula [47]

$$\gamma_{se} = 0.016(E_{iz} - 2\varphi), \quad (17)$$

where γ_{se} is the secondary electron emission coefficient, E_{iz} is the ionization energy of the impacting ion, $\varphi = 4.55$ eV is the work function of the W electrode [48]. The ionization energy for H_2^+ , H^+ , H_2O^+ , O^+ and O_2^+ are 15.4 [49], 13.6 [50], 12.65 [51], 13.61 [52] and 12.06 eV [53], respectively. The γ_{se} of H_3^+ , OH^+ and water clusters are assumed to be equal to H_2^+ , H^+ and H_2O^+ . The secondary electron emission coefficient at the plasma-liquid interface is typically two to three orders of magnitude lower than the one for metal electrodes [54], and is neglected in the model.

The species fluxes at the cathode and the plasma-liquid interface for neutrals, ions, electrons and the electron energy are [55–57]

$$\Gamma_\alpha \cdot \hat{\mathbf{n}} = \frac{1 - r_\alpha}{1 + r_\alpha} \frac{1}{2} v_{th,\alpha} n_\alpha, \quad (18)$$

$$\Gamma_i \cdot \hat{\mathbf{n}} = \frac{1 - r_i}{1 + r_i} \left(\frac{1}{2} v_{th,i} n_i + n_i (\mu_i \cdot \mathbf{E}) \cdot \hat{\mathbf{n}} \right), \quad (19)$$

$$\begin{aligned} \Gamma_e \cdot \hat{\mathbf{n}} = & \frac{1 - r_e}{1 + r_e} \left(\frac{1}{2} v_{th,e} n_e - n_e (\mu_e \cdot \mathbf{E}) \cdot \hat{\mathbf{n}} \right) \\ & - \sum_i \gamma_{se,i} (\Gamma_i \cdot \hat{\mathbf{n}}), \end{aligned} \quad (20)$$

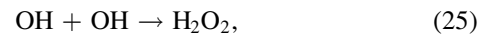
and

$$\begin{aligned} \Gamma_\epsilon \cdot \hat{\mathbf{n}} = & \frac{1 - r_\epsilon}{1 + r_\epsilon} \left(\frac{5}{6} v_{th,e} n_e - n_e (\mu_e \cdot \mathbf{E}) \cdot \hat{\mathbf{n}} \right) \\ & - \frac{5}{3} \sum_i \gamma_{se,i} \bar{\epsilon}_i (\Gamma_i \cdot \hat{\mathbf{n}}), \end{aligned} \quad (21)$$

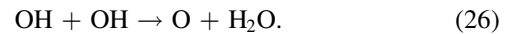
where r_α , r_i , r_e and r_ϵ are the boundary reflection coefficients for neutrals, ions, electrons and the electron energy, respectively. v_{th} is the thermal velocity

$$v_{th,j} = \sqrt{\frac{8k_B T_j}{\pi m_j}}, \quad (22)$$

where T_j and m_j are the temperature and mass of species j , respectively. The mean energy of secondary electrons emitted from surface is assumed as $\bar{\epsilon}_i = E_{iz,i} - 2\varphi$. At the cathode, the r_i for negative ions is set to unity since the negative ions are repelled by the negative potential. For positive ions, it is assumed that $r_i = 0$ at the cathode and the positive ions return as their neutral counter-part. For positive water cluster ions, they are assumed to return as basic fragments (O_2 or H and $n \times \text{H}_2\text{O}$) at the cathode. For electrons, assuming that all electrons reaching the cathode contribute to the discharge current and $r_{e,c} = 0$. The reactive neutral species of H , O and OH are assumed to recombine on the cathode as



and



The data concerning these neutral particle-surface reaction possibilities at atmosphere are scarce, most of these values are measured under low pressures [58]. Here, the reaction possibility of neutral particle-surface reactions, $\gamma_\alpha = 1 - r_\alpha$, is set to unity in the base case simulation.

At the plasma-liquid interface, r_i for negative and positive ions are set to zero and unity, respectively, contrary to the case at the cathode, and the negative ions are assumed to be absorbed by the liquid. The transport of electrons across the plasma-liquid interface is still not fully understood [57], albeit some pioneering experimental work have been performed [59, 60]. Here, the sticking coefficient of electrons at the liquid anode, $\gamma_{e,a} = 1 - r_{e,a}$, is set to unity due to the high

Table 2. Species considered in the cathodic plasma electrolysis model.

| Species | Neutral | Positive | Negative |
|----------------|-----------------------------------------------------------------------|--------------------------------------------------------------------------------------------------------------------------------------|----------------------------------------------------------------------------|
| H-species | H, H ₂ , H(2p), H(2s) | H ⁺ , H ₂ ⁺ , H ₃ ⁺ | H ⁻ |
| O-species | O, O ₂ , O ₃ , O ₂ (a) | O ⁺ , O ₂ ⁺ | O ⁻ , O ₂ ⁻ , O ₃ ⁻ |
| OH-species | OH, H ₂ O, HO ₂ , H ₂ O ₂ | OH ⁺ , H ₂ O ⁺ , H ₃ O ⁺ | OH ⁻ |
| Water clusters | | H ₂ O ₃ ⁺ , H ₄ O ₂ ⁺ , H ₅ O ₂ ⁺ | |
| Others | | | e |

kinetic energy of electrons. The sticking coefficient of electron energy, $\gamma_e = 1 - r_e$, is set as unity, by assuming all the electron energy coming from the bulk is absorbed by the interface [57]. The metastable neutrals are assumed to be de-excited at the plasma-liquid interface, that is, $\gamma_m = 1 - r_m = 1$. The transport rate of gas phase species into the liquid is determined by Henry's law [61]. However, the primary loss channel for the neutral species should be losing to the ambient air instead of dissolving into the liquid. It is assumed that the sticking coefficient $\gamma_\alpha = 0$ for most of the neutral species at the plasma-liquid interface, except H₂O₂, which has a much higher Henry's law constant than the other neutral species and is assumed to be dissolved in the liquid with a sticking coefficient of $\gamma_{\text{H}_2\text{O}_2} = 1 - r_{\text{H}_2\text{O}_2}$. The influence of the uncertainty of γ_α and γ_e on the discharge characteristics will be discussed in section 4.2.1.

3.4. Reaction chemistry

The plasma chemistry of discharge in humid air is very complicated. Generally, the discharge involves dozens of species and the reactions between these species could be up to hundreds, even thousands [62–65]. For the cathodic PE studied here, the contribution of air species to the discharge can be neglected because most of the discharge region is under the liquid level, and maintained by the water vapor evaporation from the electrolyte. In addition, as stated at the beginning of section 3, the glycerol and the NaHCO₃ in the electrolyte do not play a major role in the discharge and are neglected in the model as well. The main products in cathodic PE are assumed to be dissociated from water. Thus, only water-related species are considered. The species and reactions included in the model are summarized in tables 2 and 3, respectively.

There are 29 species and 84 reactions considered in the model. The chemical reactions are adopted from the reduced chemistry reaction set provided by Gaens and Bogaerts [65], where sensitivity analysis has been performed over a broad parameter range. In this reduction, only the reactions that contribute for more than 10% to the formation or destruction of a species were selected to reduce the number of reactions. The electron-impact reactions are characterized by the corresponding cross section data.

3.5. Numerical procedure

Due to the uncertainty of some of the above-mentioned parameters, the selection of these parameters needs to be

described in detail. Table 4 demonstrates the typical input parameters for a base case simulation of cathodic PE discharges. The working pressure of the discharge is set as $p = 1$ atm, the contact area between the cathode wire and the plasma is $S = 2\pi r_l l \approx 31.4$ mm. The discharge current I_d measured in experiment remains at around 0.3 A in the voltage range from 170 to about 300 V. The vapor layer thickness and the gas temperature are expected to vary with the discharge process. A layer thickness of $d = 200$ μm [21] is selected as the typical value. The gas temperature T_g is expected to be a little higher than the Leidenfrost temperature, that is, around 500 K. In the simulation, for a given vapor layer thickness d and a given gas temperature T_g , an appropriate set of the ballast resistance R_b and the discharge voltage V_d is required to obtain the desired discharge current of 0.3 A.

The loss rate of neutral species from the discharge region to the ambient air, k_{loss} , can be estimated from the discharge current and the experimentally measured chemical yields as follows. In the simulation, the total generation rate of H₂ in $\text{mol}(\text{m}^{-3} \text{s}^{-1})$ is expressed as

$$R_{\text{H}_2}^{\text{tot}} = c_{\text{H}_2} k_{\text{loss}}, \quad (27)$$

where $c_{\text{H}_2} = n_{\text{H}_2}/N_A$ is the mole density of H₂ and N_A is the Avogadro's constant. According to the Faraday law, the faradaic generation rate of H₂ is

$$R_{\text{H}_2} = \frac{J_d}{2eN_A d}, \quad (28)$$

where $J_d = I_d/S$ is the discharge current density. The total chemical yield of H₂ can therefore be expressed as

$$y(\text{H}_2^{\text{tot}}) = \frac{R_{\text{H}_2}^{\text{tot}}}{R_{\text{H}_2}} \cdot y(\text{H}_2), \quad (29)$$

where $y(\text{H}_2) = 0.5$ mol (mol electron) is the faradaic yield of H₂. The excess H₂ yield, i.e. the non-faradaic yield of H₂ is

$$y(\text{H}_2^{\text{E}}) = y(\text{H}_2^{\text{tot}}) - y(\text{H}_2). \quad (30)$$

In addition to the faradaic and non-faradaic yield of H₂, there is also non-faradaic O₂ generated in the plasma reaction zone in cathodic PE discharges. The non-faradaic yield of O₂ is

$$y(\text{O}_2^{\text{E}}) = \frac{c_{\text{O}_2} k_{\text{loss}}}{R_{\text{H}_2}} \cdot y(\text{H}_2), \quad (31)$$

where c_{O_2} is the mole density of O₂. Experimentally, the yield of H₂ in cathodic PE is two to three times higher than the faradaic yield of H₂ in normal electrolysis [1], i.e. $y(\text{H}_2^{\text{tot}}) = 1.0\text{--}1.5$ mol/(mol electron), from which the loss rate of neutral species k_{loss} can be estimated. Moreover, it is

Table 3. Principal rate coefficients of cathodic plasma electrolysis.

| Reaction | Rate coefficient ($\text{m}^3 \text{s}^{-1}$) | References | Threshold (eV) |
|--------------------------------------------------------------------------------------------|---------------------------------------------------|------------|------------------------|
| $\text{e} + \text{H}_2 \rightarrow \text{e} + \text{H}_2$ | Cross section | [49] | |
| $\text{e} + \text{H}_2 \rightarrow 2\text{e} + \text{H}_2^+$ | Cross section | [49] | 15.426 |
| $\text{e} + \text{H}_2 \rightarrow \text{e} + 2\text{H}$ | Cross section | [49] | 4.52 [66] |
| $\text{e} + \text{H}_2 \rightarrow \text{H} + \text{H}^-$ | Cross section | [49] | |
| $\text{e} + \text{H}_2 \rightarrow 2\text{e} + \text{H} + \text{H}^+$ | Cross section | [49] | 18.1 |
| $\text{e} + \text{H}_2^+ \rightarrow \text{e} + \text{H} + \text{H}^+$ | Cross section | [67] | 2.4 |
| $\text{e} + \text{H}_2 \rightarrow \text{e} + \text{H} + \text{H}(2\text{s})$ | Cross section | [67] | 14.9 |
| $\text{e} + \text{H}_2 \rightarrow \text{e} + \text{H}(2\text{p}) + \text{H}(2\text{s})$ | Cross section | [67] | 23 |
| $\text{e} + \text{H} \rightarrow \text{e} + \text{H}$ | Cross section | [68] | |
| $\text{e} + \text{H} \rightarrow 2\text{e} + \text{H}^+$ | Cross section | [50] | 13.6 |
| $\text{e} + \text{H} \rightarrow \text{e} + \text{H}(2\text{p})$ | Cross section | [67] | 10.2 |
| $\text{e} + \text{H} \rightarrow \text{e} + \text{H}(2\text{s})$ | Cross section | [67] | 10.2 |
| $\text{e} + \text{H}(2\text{s}) \rightarrow \text{e} + \text{H}(2\text{p})$ | Cross section | [67] | 1.934×10^{-5} |
| $\text{e} + \text{H}(2\text{s}) \rightarrow 2\text{e} + \text{H}^+$ | Cross section | [67] | 3.4 |
| $\text{e} + \text{H}_3^+ \rightarrow 3\text{H}$ | Cross section | [67, 69] | |
| $\text{e} + \text{H}_3^+ \rightarrow \text{H}_2 + \text{H}$ | Cross section | [67, 69] | |
| $\text{e} + \text{H}_2\text{O} \rightarrow \text{e} + \text{H}_2\text{O}$ | Cross section | [70] | |
| $\text{e} + \text{H}_2\text{O} \rightarrow 2\text{e} + \text{H}_2\text{O}^+$ | Cross section | [70] | 12.65 [51] |
| $\text{e} + \text{H}_2\text{O} \rightarrow 2\text{e} + \text{H}^+ + \text{OH}$ | Cross section | [70] | 16.95 [71] |
| $\text{e} + \text{H}_2\text{O} \rightarrow 2\text{e} + \text{H} + \text{OH}^+$ | Cross section | [70] | 18.116 [72] |
| $\text{e} + \text{H}_2\text{O} \rightarrow 2\text{e} + \text{O}^+ + \text{H}_2$ | Cross section | [70] | 19 [73] |
| $\text{e} + \text{H}_2\text{O} \rightarrow 2\text{e} + \text{H}_2^+ + \text{O}$ | Cross section | [70] | 20.7 [74] |
| $\text{e} + \text{H}_2\text{O} \rightarrow \text{OH} + \text{H}^-$ | Cross section | [70] | 5.5 |
| $\text{e} + \text{H}_2\text{O} \rightarrow \text{e} + \text{OH} + \text{H}$ | Cross section | [70] | 5.1 |
| $\text{e} + \text{H}_2\text{O}^+ \rightarrow \text{O} + 2\text{H}$ | $4.9 \times 10^{-14} T_e^{-0.5}$ | [65] | |
| $\text{e} + \text{H}_2\text{O}^+ \rightarrow \text{OH} + \text{H}$ | $1.38 \times 10^{-14} T_e^{-0.5}$ | [65] | |
| $\text{e} + \text{O} \rightarrow 2\text{e} + \text{O}^+$ | Cross section | [52] | 13.61 |
| $\text{e} + \text{O}_2 \rightarrow \text{e} + \text{O}_2(a)$ | Cross section | [53] | 0.977 [75] |
| $\text{e} + \text{O}_2 \rightarrow 2\text{e} + \text{O}_2^+$ | Cross section | [53] | 12.06 |
| $\text{e} + \text{O}_2 \rightarrow \text{e} + 2\text{O}$ | Cross section | [76] | 13.5 |
| $\text{e} + \text{O}_2 \rightarrow \text{O}^- + \text{O}$ | Cross section | [77] | 4.3 |
| $\text{e} + \text{O}_2(a) \rightarrow \text{e} + 2\text{O}$ | Cross section | [65] | 12.523 |
| $\text{e} + \text{OH} \rightarrow \text{e} + \text{O} + \text{H}$ | $2.08 \times 10^{-13} T_e^{-0.76} \exp(-6.9/T_e)$ | [65, 78] | 4.77 |
| $\text{e} + \text{H}_5\text{O}_2^+ \rightarrow 2\text{H} + \text{H}_2\text{O} + \text{OH}$ | $2 \times 10^{-13} (T_g/300)^{-0.5}$ | [65] | |
| $\text{H}_2 + \text{H}_2^+ \rightarrow \text{H}_3^+ + \text{H}$ | 2.1×10^{-15} | [65, 79] | |
| $\text{H}_2^+ + \text{H} \rightarrow \text{H}_2 + \text{H}^+$ | 6.39×10^{-16} | [38] | |
| $2\text{H} + \text{H}_2 \rightarrow 2\text{H}_2$ | $4 \times 10^{-44} (T_g/300)^{-1}$ | [65] | |
| $2\text{H} + \text{O}_2 \rightarrow \text{H}_2 + \text{O}_2$ | $2 \times 10^{-44} (T_g/300)^{-1}$ | [65] | |
| $2\text{H} + \text{O}_3 \rightarrow \text{H}_2 + \text{O}_3$ | $4 \times 10^{-44} (T_g/300)^{-1}$ | [65] | |
| $2\text{H} + \text{H}_2\text{O} \rightarrow \text{H}_2 + \text{H}_2\text{O}$ | $9.2 \times 10^{-44} (T_g/300)^{-1}$ | [65] | |
| $\text{O} + \text{O}^- \rightarrow \text{e} + \text{O}_2$ | 1.5×10^{-16} | [65] | |
| $\text{O} + 2\text{O}_2 \rightarrow \text{O}_3 + \text{O}_2$ | $6.4 \times 10^{-47} \exp(663/T_g)$ | [65] | |
| $\text{O} + \text{O}_2 + \text{H}_2 \rightarrow \text{O}_3 + \text{H}_2$ | $1.3 \times 10^{-46} \exp(663/T_g)$ | [65] | |
| $\text{O} + \text{O}_2 + \text{O}_3 \rightarrow 2\text{O}_3$ | $1.3 \times 10^{-46} \exp(663/T_g)$ | [65] | |
| $\text{O} + \text{O}_2 + \text{H}_2\text{O} \rightarrow \text{O}_3 + \text{H}_2\text{O}$ | $3.2 \times 10^{-46} \exp(663/T_g)$ | [65] | |
| $\text{O} + \text{O}_2^- \rightarrow \text{O}^- + \text{O}_2$ | $1.5 \times 10^{-16} (T_g/300)^{0.5}$ | [65] | |
| $\text{O} + \text{O}_2^- \rightarrow \text{e} + \text{O}_3$ | 1.5×10^{-16} | [65] | |
| $\text{O} + \text{O}_3 \rightarrow 2\text{O}_2$ | $8 \times 10^{-18} \exp(-2060/T_g)$ | [65] | |
| $\text{O} + \text{O}_3^- \rightarrow \text{O}_2^- + \text{O}_2$ | 3.2×10^{-16} | [65] | |
| $\text{O} + \text{O}_3^- \rightarrow \text{e} + 2\text{O}_2$ | 3×10^{-16} | [65] | |
| $\text{O}^- + \text{O}_2 \rightarrow \text{O} + \text{O}_2^-$ | 1×10^{-16} | [65] | |
| $\text{O}^- + \text{O}_2 + \text{M} \rightarrow \text{O}_3^- + \text{M}$ | $1.1 \times 10^{-42} (T_g/300)^{-1}$ | [65] | |
| $\text{O}^- + \text{O}_2^+ + \text{M} \rightarrow \text{O} + \text{O}_2 + \text{M}$ | $2 \times 10^{-37} (T_g/300)^{-2.5}$ | [65] | |
| $\text{O}_2(a) + \text{O}_3 \rightarrow 2\text{O}_2 + \text{O}$ | 1×10^{-20} | [65] | |
| $\text{H} + \text{O}_2^- \rightarrow \text{H}^- + \text{O}_2$ | 7×10^{-16} | [65] | |
| $\text{H} + \text{O}_3 \rightarrow \text{OH} + \text{O}_2$ | $2.71 \times 10^{-17} (T_g/300)^{0.75}$ | [65] | |

Table 3. (Continued.)

| Reaction | Rate coefficient ($\text{m}^3 \text{s}^{-1}$) | References | Threshold (eV) |
|-------------------------------------------------------------------------------------------------------------------|---------------------------------------------------------|------------|----------------|
| $\text{H} + \text{OH}^- \rightarrow \text{e} + \text{H}_2\text{O}$ | 1.8×10^{-15} | [65] | |
| $\text{H} + \text{HO}_2 \rightarrow \text{H}_2 + \text{O}_2$ | $2.06 \times 10^{-17} (T_g/300)^{0.84} \exp(-277/T_g)$ | [65] | |
| $\text{H} + \text{HO}_2 \rightarrow 2\text{OH}$ | $1.66 \times 10^{-16} \exp(-413/T_g)$ | [65] | |
| $\text{H}^+ + \text{O} \rightarrow \text{H} + \text{O}^+$ | $3.04 \times 10^{-16} (T_g/300)^{0.47} \exp(11.5/T_g)$ | [65] | |
| $\text{H}^- + \text{O}_2 \rightarrow \text{e} + \text{HO}_2$ | 1.2×10^{-15} | [65] | |
| $\text{H}^- + \text{H}_2\text{O} \rightarrow \text{OH}^- + \text{H}_2$ | 3.8×10^{-15} | [65] | |
| $\text{OH} + \text{O} \rightarrow \text{H} + \text{O}_2$ | $1.81 \times 10^{-17} (T_g/300)^{-0.31} \exp(177/T_g)$ | [65] | |
| $2\text{OH} + \text{O}_2 \rightarrow \text{H}_2\text{O}_2 + \text{O}_2$ | $8 \times 10^{-43} (T_g/300)^{-0.9}$ | [65] | |
| $2\text{OH} + \text{H}_2 \rightarrow \text{H}_2\text{O}_2 + \text{H}_2$ | $1.6 \times 10^{-42} (T_g/300)^{-0.9}$ | [65] | |
| $2\text{OH} + \text{H}_2\text{O} \rightarrow \text{H}_2\text{O}_2 + \text{H}_2\text{O}$ | $4 \times 10^{-42} (T_g/300)^{-0.9}$ | [65] | |
| $2\text{OH} + \text{O}_3 \rightarrow \text{H}_2\text{O}_2 + \text{O}_3$ | $1.6 \times 10^{-42} (T_g/300)^{-0.9}$ | [65] | |
| $\text{OH} + \text{HO}_2 \rightarrow \text{H}_2\text{O} + \text{O}_2$ | $4.8 \times 10^{-17} \exp(250/T_g)$ | [65] | |
| $\text{OH} + \text{H}_2\text{O}_2 \rightarrow \text{H}_2\text{O} + \text{HO}_2$ | $4.53 \times 10^{-18} \exp(-288.9/T_g)$ | [65] | |
| $\text{OH}^- + \text{O} \rightarrow \text{e} + \text{HO}_2$ | $4 \times 10^{-16} (T_g/300)^{0.5}$ | [65] | |
| $\text{HO}_2 + \text{O} \rightarrow \text{OH} + \text{O}_2$ | $2.71 \times 10^{-17} \exp(224/T_g)$ | [65] | |
| $\text{H}_2\text{O} + \text{H}_2\text{O}^+ \rightarrow \text{H}_3\text{O}^+ + \text{OH}$ | 1.86×10^{-15} | [65] | |
| $\text{H}_2\text{O}^+ + \text{O}_2 \rightarrow \text{H}_2\text{O} + \text{O}_2^+$ | 3.3×10^{-16} | [65] | |
| $\text{H}_2\text{O}_2 + \text{O} \rightarrow \text{HO}_2 + \text{OH}$ | $1.79 \times 10^{-19} (T_g/300)^{2.92} \exp(-1394/T_g)$ | [65] | |
| $\text{O}_2^+ + \text{H}_2\text{O} \rightarrow \text{H}_2\text{O}_3^+$ | $8.32 \times 10^{-16} [(2.54(T_g/300)^{-0.5}) + 0.62]$ | [80] | |
| $\text{H}_2\text{O}_3^+ \rightarrow \text{O}_2^+ + \text{H}_2\text{O}$ | $3.96 \times 10^{13} [2.54(T_g/300)^{-0.5}) + 0.62]$ | [80] | |
| | $\times \exp(-7610/T_g)$ | | |
| $\text{H}_2\text{O}_3^+ + \text{H}_2\text{O} \rightarrow \text{H}_3\text{O}^+ + \text{OH} + \text{O}_2$ | 1.3×10^{-15} | [65] | |
| $\text{H}_2\text{O}_3^+ + \text{H}_2\text{O} \rightarrow \text{H}_4\text{O}_2^+ + \text{O}_2$ | 1×10^{-15} | [65] | |
| $\text{H}_4\text{O}_2^+ + \text{H}_2\text{O} \rightarrow \text{H}_5\text{O}_2^+ + \text{OH}$ | 1.4×10^{-15} | [65] | |
| $\text{H}_3\text{O}^+ + \text{H}_2\text{O} \rightarrow \text{H}_5\text{O}_2^+$ | $9.29 \times 10^{-16} [(2.54(T_g/300)^{-0.5}) + 0.62]$ | [80] | |
| $\text{H}_5\text{O}_2^+ \rightarrow \text{H}_3\text{O}^+ + \text{H}_2\text{O}$ | $1.24 \times 10^{16} [2.54(T_g/300)^{-0.5}) + 0.62]$ | [80] | |
| | $\times \exp(-16430/T_g)$ | | |
| $\text{H}_5\text{O}_2^+ + \text{O}^- + \text{M} \rightarrow \text{O} + \text{H} + 2\text{H}_2\text{O} + \text{M}$ | $2 \times 10^{-37} (T_g/300)^{-2.5}$ | [65] | |

Table 4. Input parameters for a base case simulation of cathodic PE discharge.

| Parameter | Value | Description |
|--------------------------------------------|--------------------|--------------------------------------------------------------------|
| p | 1 atm | Pressure |
| l | 5 mm | Cathode length immersed in the liquid |
| r_1 | 1 mm | Cathode wire radius |
| V_d | 250 V | Discharge voltage |
| I_d | 0.3 A | Discharge current |
| R_b | 250 Ω | Ballast resistance |
| d | 200 μm | Vapor layer thickness |
| T_g | 500 K | Vapor layer temperature |
| k_{loss} | 45 s^{-1} | Loss rate of neutral species |
| $\gamma_{\text{H}_2\text{O}_2}$ | 0.01 | Sticking coefficient of H_2O_2 at the liquid anode |
| γ_{H} | 1 | γ_{α} for reaction (23) |
| γ_{O} | 1 | γ_{α} for reaction (24) |
| γ_{OH} | 1 | γ_{α} for reaction (25) or (26) |
| γ_{m} | 1 | γ_{α} for de-excitation at the electrode surface |
| $\gamma_{\text{e,c}}, \gamma_{\text{e,a}}$ | 1 | γ_{e} of electrons at the cathode or anode |
| γ_{e} | 1 | Sticking coefficient for electron energy |
| $r_{\text{i,p,c}}$ | 0 | r_i of positive ions at the cathode |
| $r_{\text{i,p,a}}$ | 1 | r_i of positive ions at the anode |
| $r_{\text{i,n,c}}$ | 1 | r_i of negative ions at the cathode |
| $r_{\text{i,n,a}}$ | 0 | r_i of negative ions at the anode |

found that the mass balance among the non-faradaic H_2 and O_2 dissociated from H_2O is maintained in the plasma reaction zone, that is, $y(\text{H}_2^{\text{E}})/y(\text{O}_2^{\text{E}}) \approx 2$. This proportional relationship adds another constraint to the model and is used to estimate the value of boundary conditions in section 4.2.1.

The numerical procedure can be determined according to the above discussion. For a given vapor layer thickness and gas temperature, selecting the proper ballast resistance and discharge voltage to obtain the desired discharge current of 0.3 A, then modulate the boundary conditions and the loss rate k_{loss} to obtain the desired gas chemical yield ratio and the desired total chemical yield of H_2 .

4. Results and discussion

4.1. Base case simulation

The modeling results for the conditions listed in table 4 are illustrated as a base case. The parameters are selected in such a way that the experimental conditions are closely reproduced by the simulation. The uncertainties of the boundary conditions and the loss rate of neutral species will be discussed in section 4.2. Figure 4 shows the modeled distributions of space

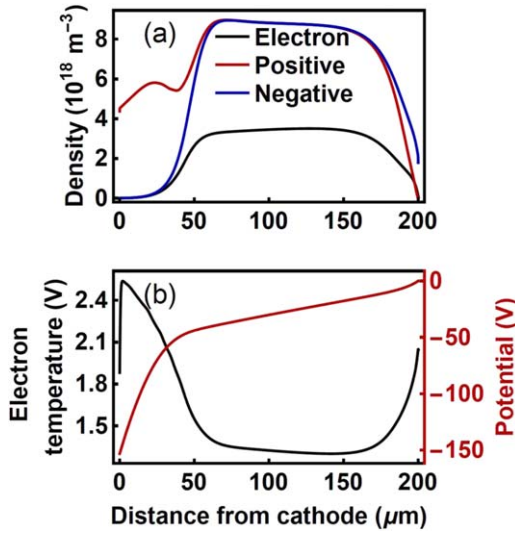


Figure 4. The distributions of (a) space charge densities and (b) electron temperature and potential for the base case simulation using the input parameters listed in table 4.

charge densities, electron temperature and potential across the vapor layer. All the following results are at their steady states. From figure 4(a) the plasma is highly electronegative. The electron density has a similar profile to the negative charge density, but the maximum is about 40% of the latter. By assuming the sheath thickness as the position at which the negative charge density (or positive charge density, whichever is lower) is 95% of the positive charge density (or negative charge density), the cathode and anode sheath thicknesses can be evaluated as about 50 and 20 μm , respectively. The bulk plasma density distributions are uniform but slightly asymmetric, with their maximum of about $9 \times 10^{18} \text{ m}^{-3}$ closer to the cathode than to the anode. Figure 4(b) shows that the electron temperature T_e exhibits peaks in the cathode and anode sheath, up to 2.5 and 2.1 V, respectively, and low values of about 1.3 V in the bulk plasma region. The high electron temperatures in the sheath can be attributed to the electron acceleration in the electric field, accumulating energy, until the energy is above the inelastic collision thresholds and thereby losing energy rapidly. The potential drop across the vapor layer is about 160 V, and this value is insensitive to the input parameters except the vapor layer thickness, which will be discussed in section 4.3. The reduced electric field E/N in the bulk plasma region is relatively low, around 20 Td, due to the high pressure. The highly electronegative plasma under low E/N obtained here is consistent with the observation by Avtaeva *et al* [39]. The transient evolution of the plasma parameters is not discussed in detail but briefly described below. At the beginning of the discharge (a few nanoseconds), the number density of each species increases rapidly in the bulk plasma region, the electric field near the electrode is enhanced to form a cathode sheath. As the discharge goes on, at about $10^{-5} - 10^{-4} \text{ s}$, the electron temperature and potential have reached a relatively stable state, the profiles are similar to that of figure 4(b). The evolution of the number density of each species is more

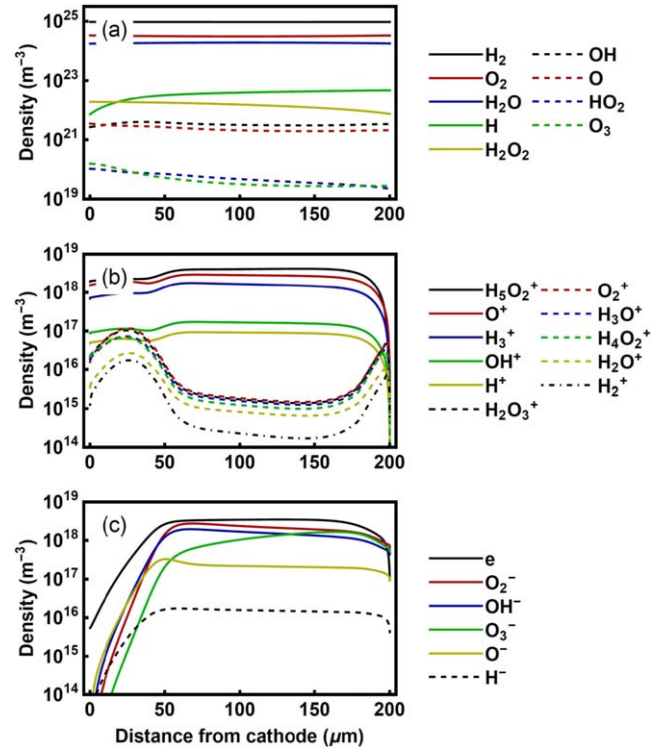


Figure 5. The distributions of (a) neutral species, (b) positive ions and (c) negative ions for the base case simulation using the input parameters listed in table 4.

complicated. In general, the plasma is always highly electronegative. The positive and negative space charge densities reach 10^{20} m^{-3} at 10^{-5} s , then gradually decrease. The electron density is always lower than 10^{19} m^{-3} . At 10^{-1} s , all the plasma parameters achieve their steady states, as shown in figure 4.

The modeled number densities of each species are demonstrated in figure 5. Figure 5(a) shows that the primary neutral species in cathodic PE discharges are H_2 and O_2 dissociated from H_2O . The number density of O_2 is about half of H_2 , obeying the mass balance. The dissociation degree of H_2 and O_2 , that is, the ratio of atomic over molecular species, is lower than 1%. The primary positive ions are H_5O_2^+ , O^+ and H_3^+ , on the order of 10^{18} m^{-3} , as shown in figure 5(b). The number densities of OH^+ and H^+ are lower, around the order of 10^{17} m^{-3} . The primary negative ions are O_2^- , O^- and OH^- near the cathode sheath, and O_2^- , O_3^- and OH^- near the plasma-liquid interface. The number densities of these negative ions are on the same order to the electrons, except in the cathode sheath, since the electron has a much higher thermal velocity. All the negative species have a similar profile.

The H lines and OH bands have been observed in the emission spectra of cathodic PE [3, 14]. However, there have been few published data on the diagnosis of cathodic PE, and the results of electron density are mostly in the range of $10^{20} - 10^{21} \text{ m}^{-3}$ [14, 81], which is higher than the modeled electron density on the order of $10^{18} - 10^{19} \text{ m}^{-3}$. This deviation may be caused by the following reasons. First, the discharge states of PE in our model is different from that reported in the above literature. For example, Stojadinovic

et al [14] investigated the characteristics of cathodic PE by optical emission spectroscopy (OES) in recent years. The metal cathode is tungsten or nickel, in a mixed solution of ethylene glycol, water and borax. The electron density estimated using the Stark broadening of H_α and H_β line profiles are $(7 \pm 3) \times 10^{20} \text{ m}^{-3}$ and $(7 \pm 3) \times 10^{21} \text{ m}^{-3}$, corresponding to the microdischarge/liquid interface region and the region near the cathode surface. However, the discharge process is physical-dominated and micro-arc discharges take place on the electrode surface. This can be inferred from the electrode surface after the discharge, which is very rough and covered with grains, channels, and holes. When the discharge process is chemical-reaction-dominated (as described in our model), the electron density is expected to be much lower. Secondly, the most popular plasma diagnostic tool for PE is Stark broadening spectroscopic method based on OES, which is not suitable for measuring electron densities lower than 10^{20} m^{-3} [82, 83]. Therefore, the results of electron density lower than 10^{20} m^{-3} require other methods and are rarely reported. For example, Slovetskii *et al* [22] evaluated an electron density of $1\text{--}3 \times 10^{18} \text{ m}^{-3}$ of PE discharge from the measured field strengths. For a typical PE, the electrode cannot be fully covered by the micro-arc discharges, resulting in the locally focused currents, as well as the higher local electron density and temperature [14]. When the discharge process is chemical-reaction-dominated, a stable glow discharge takes place with a relatively low electron density, with a magnitude similar to the microdischarges under similar discharge conditions [84, 85].

4.2. Influence of the undetermined parameters

4.2.1. Influence of boundary conditions on the gas chemical yield ratio.

In plasma simulation, boundary conditions are of key importance in determining the production and destruction of each species. However, the fundamental data for particle-surface reaction probabilities in atmospheric plasmas are scarce [58], as well as for the transport of electrons across the plasma-liquid interface [57]. Therefore, the influence of the uncertainty of boundary conditions on modeling results needs to be considered and is discussed as follows.

As mentioned in section 3.3, the neutral species are assumed to be reflected at the plasma-liquid interface except H_2O_2 . The influence of the sticking coefficient $\gamma_{\text{H}_2\text{O}_2}$ is shown in figure 6. Figure 6(a) shows that, as $\gamma_{\text{H}_2\text{O}_2}$ increases, the number density of H_2O_2 decreases, especially near the plasma-liquid interface where H_2O_2 is dissolved into the liquid. The non-faradaic chemical yield ratio of $y(\text{H}_2^{\text{E}})/y(\text{O}_2^{\text{E}})$ is strongly influenced by $\gamma_{\text{H}_2\text{O}_2}$, as shown in figure 6(f). The dissolved H_2O_2 is replaced by H_2O in the model, which means that the loss of O species is increased with $\gamma_{\text{H}_2\text{O}_2}$. When $\gamma_{\text{H}_2\text{O}_2} = 0.01$, the ratio is about 2, which satisfies the constraint of mass balance in the plasma reaction zone [3], and is therefore selected in the base case simulation as listed in table 4. It has been found that the choice of surface reaction probabilities of neutral particles, such as H, O and OH, has significantly influence on the computed species densities [58].

Figures 6(b)–(d) shows the number densities of H, O and OH as a function of their sticking coefficients on the cathode. The choice of surface reaction coefficients can strongly influence the species number densities. As increasing the sticking coefficients of O, H and OH from 0 to 1, the corresponding species number densities are significantly decreased near the cathode surface. Figure 6(e) also shows the influence of electron sticking coefficient at the plasma-liquid interface on the electron density. Similar to the results of Lindsay *et al* [57], the electron densities near the cathode and in the bulk plasma region are barely influenced. Increasing $\gamma_{\text{e,a}}$ eliminates the accumulation of electrons on the plasma side of the plasma-liquid interface and the decline of electron density could be more than five orders of magnitude. However, albeit the number densities of H, O, OH and electron are decreased with their sticking coefficients, the chemical yield ratio of H_2 to O_2 is barely affected. Thanks to the insensitivity of the yield ratio to these boundary conditions, the sticking coefficients listed in table 4 can be set as the typical parameters in cathodic PE discharges.

4.2.2. Influence of k_{loss} on the chemical yield of H_2 .

Another undetermined parameter in the model is the loss rate of neutral species k_{loss} . As mentioned in section 3.1, k_{loss} can be conveniently estimated by comparing the modeled and the experimentally measured gas yields. Figure 7 shows that the total chemical yield of H_2 calculated from equation (29), $y(\text{H}_2^{\text{E}})$, increases linearly with k_{loss} , which is expected from equation (27). To obtain the modeled $y(\text{H}_2^{\text{tot}})$ in the range of 1.0–1.5, the corresponding range of k_{loss} is from 30 to 50 s^{-1} . The chemical yield ratio of $y(\text{H}_2^{\text{E}})/y(\text{O}_2^{\text{E}})$ is less influenced by k_{loss} , in the range from 1.7 to about 2. Here, $k_{\text{loss}} = 45 \text{ s}^{-1}$ is selected as a typical value in the base case simulation. At $k_{\text{loss}} = 45 \text{ s}^{-1}$, the model gives a total H_2 yield of $y(\text{H}_2) = 1.43 \text{ mol}/(\text{mol electron})$, the gas yields in excess of the Faraday law are $y(\text{H}_2^{\text{E}}) = 0.93 \text{ mol}/(\text{mol electron})$ and $y(\text{O}_2^{\text{E}}) = 0.48 \text{ mol}/(\text{mol electron})$, respectively. These values are similar to the experimental results of $y(\text{H}_2) = 1.37 \text{ mol}/(\text{mol electron})$, $y(\text{H}_2^{\text{E}}) = 0.87 \text{ mol}/(\text{mol electron})$ and $y(\text{O}_2^{\text{E}}) = 0.46 \text{ mol}/(\text{mol electron})$ [1, 3, 19], and the experimental conditions are similar to that used in this model. It should be noted that the chemical yields of H_2 and O_2 are not quite sensitive to the conditions. Therefore, the chemical yields of H_2 and O_2 are assumed to be the same in physical-dominated and chemical-reaction-dominated PE discharges. The earlier reports on the chemical effects of cathodic PE showed that only H_2 and O_2 are liberated at the cathode [3]. These results are consistent with our modeling results, that the concentration of H_2O_2 is about three orders of magnitude lower than H_2 and O_2 (see figure 6(a)). In acid catholyte solution (e.g. KHSO_4), distinct formation of H_2O_2 was observed, demonstrating that the liquid-phase reaction zone of cathodic PE does contribute to its total non-faradaic yields [3]. However, since only the plasma reaction zone is

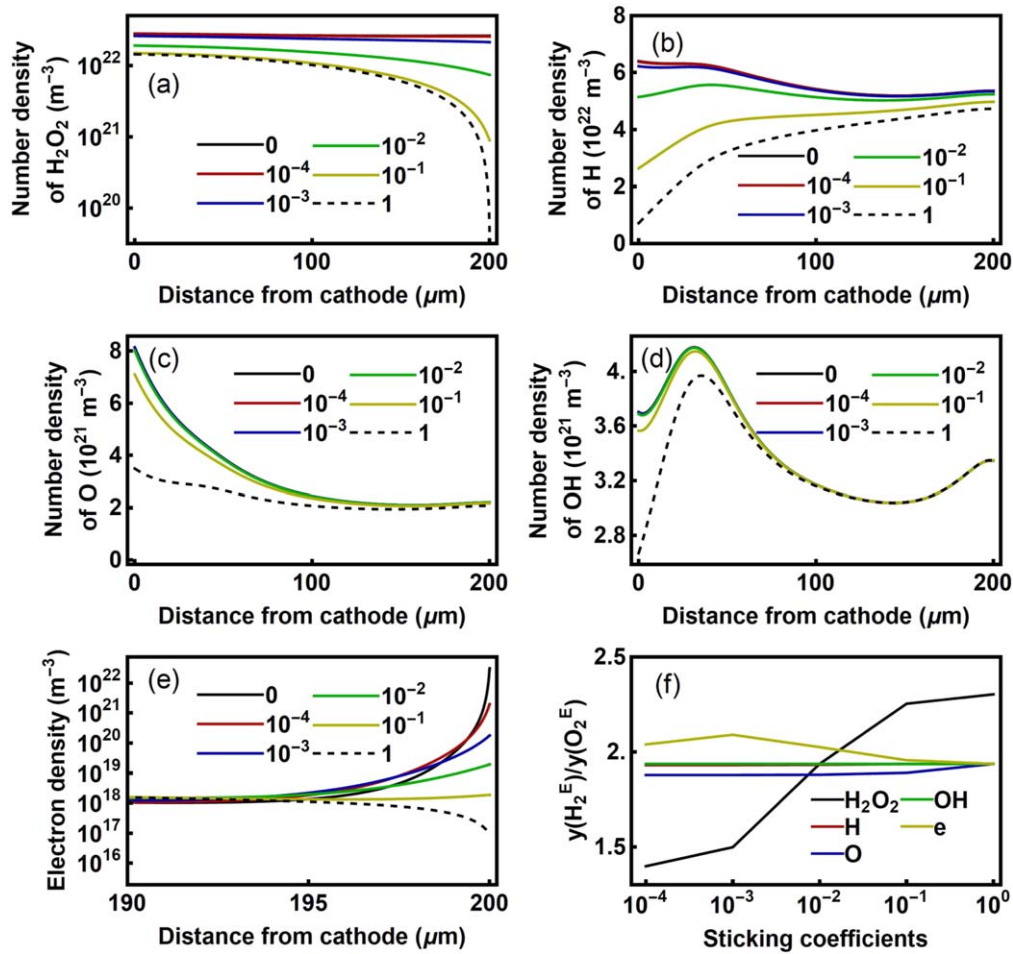


Figure 6. Species number densities as a function of the corresponding sticking coefficients for (a) $\gamma_{\text{H}_2\text{O}_2}$, (b) γ_{H} , (c) γ_{O} , (d) γ_{OH} , (e) $\gamma_{\text{e,a}}$, and (f) their influence on the non-faradaic chemical yield ratio of $y(\text{H}_2^E)/y(\text{O}_2^E)$.

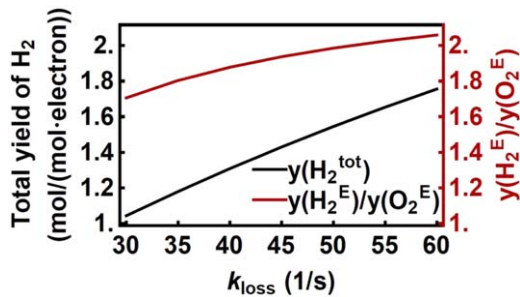


Figure 7. Influence of loss rate k_{loss} on the total yield of H₂, $y(\text{H}_2^{\text{tot}})$, and the non-faradaic chemical yield ratio of $y(\text{H}_2^E)/y(\text{O}_2^E)$.

considered in this model, the H₂O₂ formation in the catholyte solution is not included and discussed here.

4.3. Influence of vapor layer thickness and gas temperature

The variation of vapor layer thickness, in the range of dozens to hundreds of μm, is determined by the thermal energy gain and loss. The thermal energy obtained from the cathode surface is then dissipated to the ambient air and the electrolyte. It has been found that the vapor layer thickness is nearly proportional to the applied voltage, due to the high Joule

heating from the electrode [21]. In this simulation, the plasma-liquid interface is assumed to be fixed during each calculation, and different vapor layer thickness is simulated to investigate its influence on the modeling results.

Figure 8 illustrates the spatial distributions of electron density, electron temperature and potential with different vapor layer thickness d . For each value of d , the ballast resistance R_b is set as 250 Ω, an appropriate discharge voltage V_d was selected to obtain the desired discharge current of $I_d = 0.3$ A, then $\gamma_{\text{H}_2\text{O}_2}$ and k_{loss} were modulated to obtain the desired $y(\text{H}_2^{\text{tot}})$ and $y(\text{H}_2^E)/y(\text{O}_2^E)$. Figure 8(a) shows a maximum electron density of about $1 \times 10^{18} \text{ m}^{-3}$ at $d = 50 \mu\text{m}$. The maximum electron density increases with the vapor layer thickness d and saturates at around $3.8 \times 10^{18} \text{ m}^{-3}$. When d is less than 100 μm, the discharge is significantly suppressed due to the vapor layer thickness approaching the cathode sheath thickness and the bulk plasma region being reduced. When d is greater than 100 μm, the plasma can be fully developed. Further increasing the layer thickness only contribute to the widening of the bulk plasma region, which can be identified by the high electron density around $3.8 \times 10^{18} \text{ m}^{-3}$ in figure 8(a) and the low electron temperature around 1.3 V in figure 8(b).

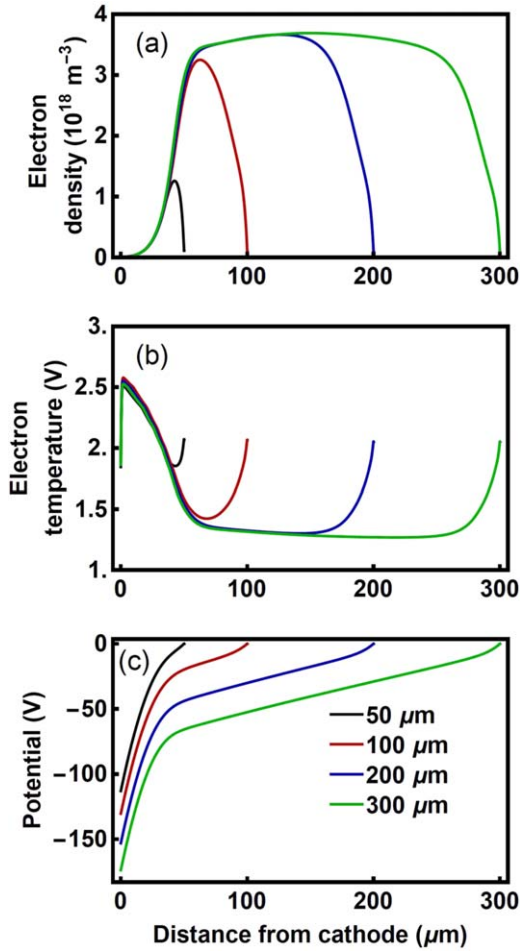


Figure 8. Distributions of (a) electron density, (b) electron temperature and (c) potential across the vapor layer as a function of the vapor layer thickness.

For a given vapor layer thickness, the modeled discharge current is primarily determined by the discharge voltage V_d and the ballast resistance R_b , and is insensitive to other parameters. According to Kirchhoff's voltage law, the discharge voltage should be the sum of the potential drop across the vapor layer and the potential drop in the electrolyte, that is

$$V_d = V_p + R_b \cdot I_d. \quad (32)$$

The ballast resistance R_b is a constant, and the discharge current I_d remains unchanged in the voltage range from 170 to about 300 V as shown in figure 2. Therefore, the variation of discharge voltage V_d in this range can be attributed to the variation of V_p . The choice of R_b is not a crucial factor, since the appropriate V_d increases linearly with R_b . From a modeling perspective, V_p is insensitive to all the input parameters except the vapor layer thickness d . Figure 8(c) also illustrates the potential profiles across the vapor layer at different layer thicknesses. The potential profiles are similar, about more than 100 V drops in the cathode sheath and about 10 V in the anode sheath region. The electric fields in the bulk plasma region are almost the same, while the potential drops across the cathode and anode sheath are barely changed, therefore a higher potential drop V_p is observed with a wider layer

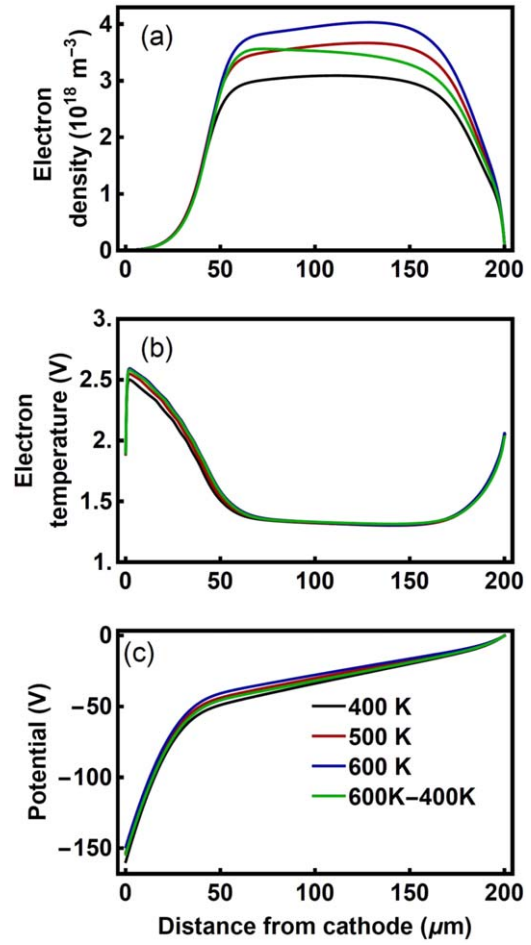


Figure 9. Distributions of (a) electron density, (b) electron temperature and (c) potential across the vapor layer as a function of the gas temperature.

thickness d . In addition, the potential drop V_p increases linearly with the vapor layer thickness d when the plasma can be fully developed ($d > 100 \mu\text{m}$), which is consistent with the experimental measurements [21]. From above results, it can be suggested that in the stable discharge region from 170 V to about 300 V, the vapor layer thickness increases with the discharge voltage due to the increased Joule heating. The constant electric field in the widening bulk plasma region increases the potential drop across the vapor layer, which consumes the increased voltage and keeps the discharge current at around 0.3 A.

The influence of gas temperature is also investigated, as shown in figure 9. The gas temperature is expected to be around the Leidenfrost temperature of tungsten/electrolyte, that is, higher than the boiling point of water, 373 K, and lower than the Leidenfrost temperature of tungsten/water, 543 K. Here, a constant gas temperature T_g ranging from 400 to 600 K is selected. However, gradients of gas temperature are expected at the edges, which could affect the number densities of species. To demonstrate the effects of T_g gradients, the model is also performed with a T_g that varies linearly from 600 K at the electrode to 400 K at the plasma/liquid boundary. With the increase of T_g , the number densities

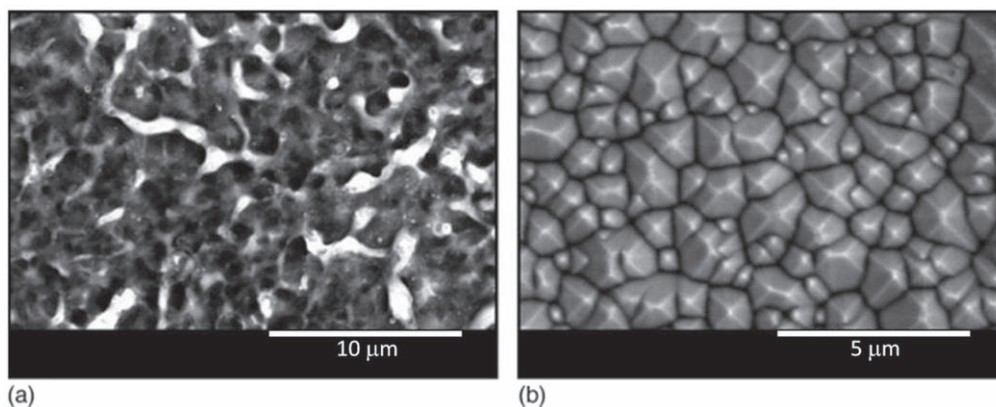


Figure 10. (a) Porous and (b) textured Si wafer obtained by PE using electrolyte with glycerol:water ratios of (a) 5:1 and (b) 10:1. In both cases, a mirror-polished Si wafer was used as cathode.

of the neutral species are reduced while the potential profile is barely changed (figure 9(c)), resulting in an increased E/N . The electronegativity of the plasma is weakened under higher E/N [39]. Therefore, the electron density in the bulk plasma region increases with the gas temperature T_g , as shown in figure 9(a), while the number densities of negative ions are relatively reduced (data not shown here). The electron temperature and potential shown in figures 9(b) and (c), as well as other discharge parameters, are barely changed with T_g . The spatially varying T_g has not much influence on the results, which are all within the upper and lower limits given by the results of 600 and 400 K. Therefore, it is concluded that the fluctuation of T_g in the possible range has no great influence on the discharge process.

4.4. Decoupling of physical processes and chemical reactions

Cathodic PE discharges are typically dominated by physical processes, and micro-arcs may form on the electrode surface due to the local current concentration induced by electro-thermal instability [5]. However, it has been found that in a cathodic PE discharge with deionized water, glycerol and 1 wt% NaHCO_3 , by changing the glycerol:water volume ratio from 5:1 to 10:1, the cathodic PE transforms from physical-dominated to chemical-dominated [25]. As shown in figure 10, at the volume ratio of 5:1, a porous structure of the cathodic surface was obtained following PE treatment, due to the strong physical interactions around the cathode. At the volume ratio of 10:1, the cathode surface illustrated a textured surface dominated by pyramidal structures, which can only be created by anisotropic chemical etching. The very different morphologies imply that the physical processes and the chemical reactions can be decoupled under certain conditions in cathodic PE discharges, and the decoupling mechanism is discussed as follows.

It has been suggested that the solvent vaporization near the electrode by Joule heating and the onset of Taylor–Helmholtz hydrodynamic instability are the primary reasons for the breakdown of normal electrolysis [1, 3, 4]. The vapor layer over the electrode is initially unstable, oscillating between expansion and shrinkage. Once the electrode reaches

the Leidenfrost temperature, the vapor layer develops into a stable form, marks the onset of film boiling. Berenson [29] theoretically studied the influence of various parameters on the minimum film boiling temperature. A proportional relationship between the minimum film boiling temperature and the surface tension of the liquid is expected, since a higher heat flux is required to overcome the higher surface tension for the onset of nucleate boiling. By increasing the glycerol/water volume ratio, the surface tension of the mixture is reduced, resulting in a lower Leidenfrost temperature, and it is easier to form a continuous and stable vapor layer.

Viscosity is another important factor that influence the decoupling of physical processes and chemical reactions in cathodic PE discharges. The viscosity of the glycerol is more than three orders of magnitude higher than the water viscosity (see table 1). The high viscosity may suppress the physical processes such as bubble implosion and shock wave. In addition, it has been found that an increase in the viscosity leads to a stabilizing effect. Increasing the mass concentration of glycerol to greater than 60% can prevent spontaneous explosions [86]. Besides, the high boiling point of glycerol reduces the generation of gas bubbles, as well as the localized intensive physical interactions.

When the physical processes are suppressed, the PE discharge is chemical-reaction-dominated. The NaHCO_3 in the electrolyte is added with the primary purpose of increasing the conductivity, albeit it may partially contribute to the chemical etching, under sufficient etching time (10–40 min) and concentration (5–25 wt%) [87]. However, the processing time of the cathodic PE is only a few seconds with much diluted NaHCO_3 , and the created pyramids has even larger sizes compared with a pure chemical etching over 10 min. In that case, other chemical etching mechanisms needs to be considered.

As shown in figure 5, there are various reactive species generated around the cathode in cathodic PE discharges. Silicon can be oxidized by H_2O_2 [88] and OH decomposed from H_2O_2 [89]. The generated SiO_2 can then be etched by H^+ [90]. Otherwise, a high etch rate for hydrogenated amorphous silicon (a-Si:H) and microcrystalline silicon was achieved by atomic hydrogen [91] and by hydrogen plasmas

[92]. Once the electrode surface is textured, the vapor layer may be further stabilized [93], which promotes the etching process in turn. A more elaborate explanation of the etching mechanism requires a more detailed knowledge of surface chemistry, which needs to be further investigated.

5. Conclusions

The cathodic PE discharge process is investigated using a one-dimensional plasma fluid model with constraint conditions obtained from the experiments. The model is developed under the conditions when the physical interactions between the plasma and the working electrode is suppressed, and the discharge is chemical-reaction-dominated. The modeling results demonstrate a high plasma density on the order of 10^{19} m^{-3} and a low electron temperature of about 1.2–1.3 eV in the bulk plasma region. The plasma is highly electro-negative, and the dominant neutral species are H_2 and O_2 dissociated from water vapor. The primary positive ion species are water cluster H_5O_2^+ , O^+ and H_3^+ , and the primary negative ion species are O_2^- , O^- , OH^- and O_3^- . The influence of the uncertainty of some input parameters are discussed. The sticking coefficient of H_2O_2 at the plasma-liquid interface and the loss rate of neutral species to the ambient air are the key parameters that determine the non-faradaic chemical yield ratio of H_2/O_2 and the total yield of H_2 . A linear relationship between the discharge voltage and the vapor layer thickness is predicted in the stable discharge region, due to the high Joule heating from the working electrode. A vapor layer thickness greater than $100 \mu\text{m}$ is required to obtain a fully developed cathodic PE discharge. The fluctuation of gas temperature has no great influence on the discharge process.

It has been found that with the increase of glycerol/water ratio in the electrolyte, the physical processes and the chemical reactions could be decoupled, and a textured electrode surface could be created through a chemical-reaction-dominated process instead of an irregular porous surface produced by the physical-dominated interactions. The decoupling mechanisms are attributed to the lower surface tension of glycerol, which reduces the Leidenfrost temperature and promotes the formation of a stable vapor layer; the higher viscosity of glycerol, which stabilizes the plasma-liquid interface and suppresses the physical interactions between the plasma and the working electrode; and the high boiling point of glycerol, which reduces the gas bubbles generation as well as the localized intensive physical interactions. The formation of a textured surface is attributed to the anisotropic chemical etching on the silicon electrode by the reactive species generated in the plasmas.

Acknowledgments

This work was supported by the National Science Foundation awards #1700787.

ORCID iDs

Bocong Zheng  <https://orcid.org/0000-0002-6052-3693>

References

- [1] Gupta S K S 2015 *Plasma Sources Sci. Technol.* **24** 063001
- [2] Bruggeman P J et al 2016 *Plasma Sources Sci. Technol.* **25** 053002
- [3] Gupta S K S and Singh R 2016 *Plasma Sources Sci. Technol.* **26** 015005
- [4] Sengupta S K, Srivastava A K and Singh R 1997 *J. Electroanal. Chem.* **427** 23
- [5] Toriyabe Y, Watanabe S, Yatsu S, Shibayama T and Mizuno T 2007 *Appl. Phys. Lett.* **91** 041501
- [6] Mariotti D and Sankaran R M 2010 *J. Phys. D: Appl. Phys.* **43** 323001
- [7] Chen Q, Li J and Li Y 2015 *J. Phys. D: Appl. Phys.* **48** 424005
- [8] Yerokhin A, Nie X, Leyland A, Matthews A and Dowey S 1999 *Surf. Coat. Technol.* **122** 73
- [9] Meletis E, Nie X, Wang F and Jiang J 2002 *Surf. Coat. Technol.* **150** 246
- [10] Kellogg H H 1950 *J. Electrochem. Soc.* **97** 133
- [11] Hickling A and Ingram M D 1964 *Trans. Faraday Soc.* **60** 783
- [12] Gupta P, Tenhundfeld G, Daigle E and Ryabkov D 2007 *Surf. Coat. Technol.* **201** 8746
- [13] Tyurin Y and Pogrebnjak A 2001 *Surf. Coat. Technol.* **142**–**144** 293
- [14] Stojadinović S, Jovović J, Tadić N, Vasilić R and Sisović N M 2015 *Europhys. Lett.* **110** 48004
- [15] Dunleavy C, Golosnoy I, Curran J and Clyne T 2009 *Surf. Coat. Technol.* **203** 3410
- [16] Bruggeman P, Schram D, González M Á, Rego R, Kong M G and Leys C 2009 *Plasma Sources Sci. Technol.* **18** 025017
- [17] Hussein R O, Nie X, Northwood D O, Yerokhin A and Matthews A 2010 *J. Phys. D: Appl. Phys.* **43** 105203
- [18] Bruggeman P and Leys C 2009 *J. Phys. D: Appl. Phys.* **42** 053001
- [19] Sengupta S K and Singh O P 1994 *J. Electroanal. Chem.* **369** 113
- [20] Sengupta S K 1998 *J. Electrochem. Soc.* **145** 2209
- [21] Yoon S-Y, Jang Y C, Lee S-H, Hong J W, Hong Y K and Kim G-H 2012 *Plasma Sources Sci. Technol.* **21** 055017
- [22] Slovetskii D I and Terent'ev S D 2003 *High Energy Chem.* **37** 310
- [23] Wüthrich R and Mandin P 2009 *Electrochim. Acta* **54** 4031
- [24] Parfenov E, Yerokhin A, Nevyantseva R, Gorbakov M, Liang C-J and Matthews A 2015 *Surf. Coat. Technol.* **269** 2
- [25] Zhang Z, Dubey M, Galipeau D, Fan Q H, Hoefelmeyer J D and Al-Qaradawi I Y 2013 *MRS Commun.* **3** 255
- [26] Wu J, Xue W, Wang B, Jin X, Du J and Li Y 2014 *Surf. Coat. Technol.* **245** 9
- [27] Kwon H M, Bird J C and Varanasi K K 2013 *Appl. Phys. Lett.* **103** 201601
- [28] Fau S, Bergez W and Colin C 2017 *Exp. Therm. Fluid Sci.* **83** 118
- [29] Berenson P J 1961 *J. Heat Transfer* **83** 351
- [30] Chen D H T and Thompson A R 1970 *J. Chem. Eng. Data* **15** 471
- [31] COMSOL Multiphysics 5.3 2017 *Plasma Module User's Guide* (Stockholm: COMSOL Inc.)
- [32] Ryzko H 1965 *Proc. Phys. Soc.* **85** 1283
- [33] Raizer Y P 1991 *Gas Discharge Physics* (Berlin: Springer)

- [34] Kee R J, Coltrin M E and Glarborg P 2003 *Chemically Reacting Flow: Theory and Practice* (New York: Wiley)
- [35] Hagelaar G J M and Pitchford L C 2005 *Plasma Sources Sci. Technol.* **14** 722
- [36] Dorai R and Kushner M J 2003 *J. Phys. D: Appl. Phys.* **36** 666
- [37] Soloshenko I A, Tsiolko V V, Pogulay S S, Kalyuzhnaya A G, Bazhenov V Y and Shchedrin A I 2009 *Plasma Sources Sci. Technol.* **18** 045019
- [38] Liu D X, Bruggeman P, Iza F, Rong M Z and Kong M G 2010 *Plasma Sources Sci. Technol.* **19** 025018
- [39] Avtaeva S V, General A A and Kel'man V A 2010 *J. Phys. D: Appl. Phys.* **43** 315201
- [40] Takeuchi N, Ishii Y and Yasuoka K 2012 *Plasma Sources Sci. Technol.* **21** 015006
- [41] Bobkova E S, Smirnov S A, Zalipaeva Y V and Rybkin V V 2014 *Plasma Chem. Plasma Process.* **34** 721
- [42] Verma A K, Alamatsaz A and Venkattraman A 2017 *J. Phys. D: Appl. Phys.* **50** 424005
- [43] Verma A K, Alamatsaz A and Venkattraman A 2016 *Plasma Process. Polym.* **14** 1600130
- [44] Wang Q, Economou D J and Donnelly V M 2006 *J. Appl. Phys.* **100** 023301
- [45] Kushner M J 2004 *J. Appl. Phys.* **95** 846
- [46] Kushner M J 2005 *J. Phys. D: Appl. Phys.* **38** 1633
- [47] Lieberman M A and Lichtenberg A J 2005 *Principles of Plasma Discharges and Materials Processing* (New Jersey: Wiley)
- [48] Speight J G *et al* 2005 *Lange's Handbook of Chemistry* vol 1 (New York: McGraw-Hill)
- [49] Yoon J-S, Song M-Y, Han J-M, Hwang S H, Chang W-S, Lee B and Itikawa Y 2008 *J. Phys. Chem. Ref. Data* **37** 913
- [50] Shah M B, Elliott D S and Gilbody H B 1987 *J. Phys. B: At. Mol. Phys.* **20** 3501
- [51] Snow K B and Thomas T F 1990 *Int. J. Mass Spectrom. Ion Process.* **96** 49
- [52] Laher R R and Gilmore F R 1990 *J. Phys. Chem. Ref. Data* **19** 277
- [53] Itikawa Y, Ichimura A, Onda K, Sakimoto K, Takayanagi K, Hatano Y, Hayashi M, Nishimura H and Tsurubuchi S 1989 *J. Phys. Chem. Ref. Data* **18** 23
- [54] Bruggeman P, Liu J, Degroote J, Kong M G, Vierendeels J and Leys C 2008 *J. Phys. D: Appl. Phys.* **41** 215201
- [55] Hagelaar G J M, de Hoog F J and Kroesen G M W 2000 *Phys. Rev. E* **62** 1452
- [56] Sakiyama Y and Graves D B 2007 *J. Appl. Phys.* **101** 073306
- [57] Lindsay A D, Graves D B and Shannon S C 2016 *J. Phys. D: Appl. Phys.* **49** 235204
- [58] Schröter S, Gibson A R, Kushner M J, Gans T and O'Connell D 2017 *Plasma Phys. Control. Fusion* **60** 014035
- [59] Rumbach P, Bartels D M, Sankaran R M and Go D B 2015 *Nat. Commun.* **6** 7248
- [60] Rumbach P, Bartels D M, Sankaran R M and Go D B 2015 *J. Phys. D: Appl. Phys.* **48** 424001
- [61] Tian W and Kushner M J 2014 *J. Phys. D: Appl. Phys.* **47** 165201
- [62] Gentile A C and Kushner M J 1995 *J. Appl. Phys.* **78** 2074
- [63] Sakiyama Y, Graves D B, Chang H-W, Shimizu T and Morfill G E 2012 *J. Phys. D: Appl. Phys.* **45** 425201
- [64] Murakami T, Niemi K, Gans T, O'Connell D and Graham W G 2012 *Plasma Sources Sci. Technol.* **22** 015003
- [65] Gaens W V and Bogaerts A 2013 *J. Phys. D: Appl. Phys.* **46** 275201
- [66] Hjartarson A T, Thorsteinsson E G and Gudmundsson J T 2010 *Plasma Sources Sci. Technol.* **19** 065008
- [67] Janev R, Langer W, Evans J and Post J 1987 *Elementary Processes in Hydrogen-Helium Plasmas* (New York: Springer)
- [68] Zecca A, Karwasz G P and Brusa R S 1996 *Riv. Nuovo Cimento* **19** 1
- [69] Mitchell J B A, Forand J L, Ng C T, Levac D P, Mitchell R E, Mul P M, Claeys W, Sen A and McGowan J W 1983 *Phys. Rev. Lett.* **51** 885
- [70] Itikawa Y and Mason N 2005 *J. Phys. Chem. Ref. Data* **34** 1
- [71] Lefavre D and Marmet P 1978 *Can. J. Phys.* **56** 1549
- [72] McCulloh K 1976 *Int. J. Mass Spectrom. Ion Phys.* **21** 333
- [73] Morrison J and Traeger J 1973 *Int. J. Mass Spectrom. Ion Phys.* **11** 77
- [74] Ehrhardt H and Kresling A 1967 *Z. Naturforsch. A* **22** 2036
- [75] Bogaerts A 2009 *Spectrochim. Acta B* **64** 1266
- [76] Cosby P C 1993 *J. Chem. Phys.* **98** 9560
- [77] Itikawa Y 2009 *J. Phys. Chem. Ref. Data* **38** 1
- [78] Riahi R, Teulet P, Lakhdar Z B and Gleizes A 2006 *Eur. Phys. J. D* **40** 223
- [79] Ferguson E E 1973 *At. Data Nucl. Data Tables* **12** 159
- [80] Sieck L W, Heron J T and Green D S 2000 *Plasma Chem. Plasma Process.* **20** 235
- [81] Guilpin C and Garbarz-Olivier J 1977 *Spectrochim. Acta B* **32** 155
- [82] Laux C O, Spence T G, Kruger C H and Zare R N 2003 *Plasma Sources Sci. Technol.* **12** 125
- [83] Gigos M A, González M Á and Cardeñoso V 2003 *Spectrochim. Acta B* **58** 1489
- [84] Zhang Y, Jiang W and Bogaerts A 2014 *J. Phys. D: Appl. Phys.* **47** 435201
- [85] Fu Y, Zhang P, Verboncoeur J P, Christlieb A J and Wang X 2018 *Phys. Plasmas* **25** 013530
- [86] Fletcher D F and Sigurdson M 1999 *Nucl. Eng. Des.* **189** 239
- [87] Vallejo B, González-Mañas M, Martínez-López J and Caballero M 2007 *Sol. Energy* **81** 565
- [88] Neuwald U, Feltz A, Memmert U and Behm R J 1995 *J. Appl. Phys.* **78** 4131
- [89] Ishikawa Y 2002 *Japan. J. Appl. Phys.* **41** 1324
- [90] Peña O, Muhl S, López W, Rodríguez-Fernández L and Ruvalcaba-Sil J 2010 *Thin Solid Films* **518** 3156
- [91] Wanka H N and Schubert M B 1997 *J. Phys. D: Appl. Phys.* **30** L28
- [92] Otake M, Kimura M and Oda S 1994 *Japan. J. Appl. Phys.* **33** 4442
- [93] Vakarelski I U, Patankar N A, Marston J O, Chan D Y C and Thoroddsen S T 2012 *Nature* **489** 274